

RESEARCH ARTICLE

10.1002/2017SW001675

Key Points:

- Complex seasonal and IMF control of the auroral electrojets (AEJs) is presented as a function of MLT
- Hemispheric asymmetry in AEJ response to IMF B_y during local winter
- Solar cycle modulation of the AEJs contributes a changing baseline to AEJ activity

Supporting Information:

- Supporting Information S1

Correspondence to:

A. R. A. Smith,
ashley.smith@ed.ac.uk

Citation:

Smith, A. R. A., Beggan, C. D., Macmillan, S., & Whaler, K. A. (2017). Climatology of the auroral electrojets derived from the along-track gradient of magnetic field intensity measured by POGO, Magsat, CHAMP, and Swarm. *Space Weather*, 15, 1257–1269. <https://doi.org/10.1002/2017SW001675>

Received 6 JUN 2017

Accepted 1 SEP 2017

Accepted article online 6 SEP 2017

Published online 9 OCT 2017

©2017. The Authors.

This is an open access article under the terms of the Creative Commons Attribution License, which permits use, distribution and reproduction in any medium, provided the original work is properly cited.

Climatology of the Auroral Electrojets Derived From the Along-Track Gradient of Magnetic Field Intensity Measured by POGO, Magsat, CHAMP, and Swarm

A. R. A. Smith¹ , C. D. Beggan² , S. Macmillan² , and K. A. Whaler¹

¹School of GeoSciences, Grant Institute, University of Edinburgh, Edinburgh, UK, ²British Geological Survey, Edinburgh, UK

Abstract The auroral electrojets (AEJs) are complex and dynamic horizontal ionospheric electric currents which form ovals around Earth's poles, being controlled by the morphology of the main magnetic field and the energy input from the solar wind interaction with the magnetosphere. The strength and location of the AEJ varies with solar wind conditions and the solar cycle but should also be controlled on decadal timescales by main field secular variation. To determine the AEJ climatology, we use data from four polar Low Earth Orbit magnetic satellite missions: POGO, Magsat, CHAMP, and Swarm. A simple estimation of the AEJ strength and latitude is made from each pass of the satellites, from peaks in the along-track gradient of the magnetic field intensity after subtracting a core and crustal magnetic field model. This measure of the AEJ activity is used to study the response in different sectors of magnetic local time (MLT) during different seasons and directions of the interplanetary magnetic field (IMF). We find a season-dependent hemispherical asymmetry in the AEJ response to IMF B_y , with a tendency toward stronger (weaker) AEJ currents in the north than the south during $B_y > 0$ ($B_y < 0$) around local winter. This effect disappears during local summer when we find a tendency toward stronger currents in the south than the north. The solar cycle modulation of the AEJ and the long-term shifting of its position and strength due to the core field variation are presented as challenges to internal field modeling.

1. Introduction

Among the various ionospheric and magnetospheric currents, the auroral electrojets (AEJs) are perhaps the most troublesome to describe and predict. This reflects their origin in the complex solar wind-magnetosphere interaction and subsequent magnetospheric unloading processes and coupling to varying ionospheric conductivity structure. They are highly variable with several different types of drivers, from partly stochastic variations in the solar wind, to seasonal effects caused by Earth's orbit and its rotational and magnetic axes, and to the longer-term modulation by the solar cycle. As a key component of space weather, understanding them is important both in terms of furthering space and geophysical research and for practical applications due to their role in geomagnetically induced currents (GICs) in power grids, atmospheric heating increasing drag on satellites, and disturbances to magnetic navigation systems (Gaunt, 2016; Pirjola, 2005).

The AEJs, and the associated field-aligned currents (FACs) which feed them, are challenging to deal with when modeling the internal fields (from the core and the crust). This is because they represent a large disturbance field which is both highly spatially and temporally variable and difficult to predict. This makes it difficult to either reject periods of data contaminated by these external fields or to model their effect. As they introduce noise to core and crustal field models, Cnossen (2017) and Finlay et al. (2017) point out that models of the core secular variation could be seriously contaminated in the polar regions by time-varying biases in external fields, depending on the data selection criteria used in building the models.

It is well known that interplanetary magnetic field (IMF) oriented southward in the geocentric solar magnetospheric (GSM) reference frame, that is, GSM IMF- $B_z < 0$, causes enhanced reconnection at the front of the magnetopause and so energy entry and driving of the magnetosphere, as first proposed by Dungey (1961). Although southward IMF is the strongest driver of reconnection, the transverse IMF component (GSM B_y), and solar wind velocity and density also have an effect. This has led to the development of “coupling functions”

which aim to quantify the amount of energy transfer into the magnetosphere in terms of solar wind parameters (Finch & Lockwood, 2007). As well as affecting the amount of energy entering, the B_y component also has the effect of twisting the magnetosphere such that magnetically conjugate points in each hemisphere get displaced longitudinally relative to each other (Østgaard et al. 2011). This has consequences for the release of energy from the magnetosphere to the ionosphere and back-coupling through the spatial distribution of ionospheric conductivity.

In addition to these variations in solar wind-magnetosphere coupling, there are various lag times involved between the energy input and the ionospheric response. On the dayside there are more direct responses through energy entry along the magnetic cusps, whereas on the dawnside/duskside and nightside convection-driven and substorm currents will be lagged due to the duration of energy buildup and unloading from the magnetotail. These lag times can be affected by the direction of the IMF (e.g., Browett et al., 2017) as well as its time history. Such issues complicate the local time pattern of the AEJs, which are also being driven by daily cycles in insolation-dependent conductivity.

The AEJs have seasonal patterns which are related both to the axial tilt providing a yearly oscillation in the amount of insolation in each hemisphere and to the effect, identified by Russell and McPherron (1973), of the projection of the typical IMF direction into the GSM frame increasing the activity around the equinoxes. This and other issues arising from the behavior of the solar wind are reviewed by Lockwood et al. (2016). There is also an approximately 11 year periodicity due to the solar cycle.

At high altitudes (above the ionosphere) the nondipole components of the geomagnetic field can often be ignored, but at ionospheric altitudes they become important and the interhemispheric differences (in terms of magnetic pole location, field intensity, and field inclination) play a role in magnetosphere-ionosphere coupling. This can be through several effects, including field intensity influencing ionospheric convection and precipitating particles (associated with both current sources and ionization), and different insolation patterns over magnetically conjugate regions. Issues of north-south asymmetries are reviewed by Laundal et al. (2017).

It is to be expected that the external current systems (in the magnetosphere and ionosphere) have long-term trends which reflect changes in the core field over time, being affected by its intensity and orientation and by the different temporal variations across Earth. Cnossen (2017) used theoretical considerations and simulations to derive scaling relations for external current systems as the dipole moment changes and reviewed how changes in dipole orientation and the nondipolar contributions could nontrivially affect the current systems and how they relate to north-south differences.

Ground-based magnetometers can be used to study the AEJs. This has been done extensively by utilizing the auroral electrojet (AE) activity index (Davis & Sugiura, 1966) and other indices, which are useful for their long-term availability and continuity. More complex usage of the data can be made from certain groupings of magnetometers (e.g., Pulkkinen et al., 2003) which is better suited to detailed regional studies. Recent advances with the SuperMAG project (Newell & Gjerloev, 2011), and studies which use this data set, show promise in making better use of the data. However, these approaches will ultimately be limited by spatial distribution of the ground stations with an uneven and incomplete coverage, particularly the bias toward the Northern Hemisphere. Satellite data, on the other hand, provide us with almost complete global coverage (with the exception of the polar gaps) and good latitudinal resolution, although they lose the advantage of continuous coverage that ground magnetometers have at given locations.

The AEJs have been estimated from several satellite magnetic data missions: Olsen (1996) using Magsat; Moretto et al. (2002) using Ørsted, CHAMP, and SAC-C; Ritter et al. (2003), Juusola et al. (2009), and Vennerstrom and Moretto (2013) using CHAMP; and Aakjær et al. (2016) using Swarm; among others. Vennerstrom and Moretto (2013) developed a method which tracks the estimated activity of the AEJs orbit by orbit. They applied it to 5 years of CHAMP data to produce statistical synthesis plots which show the response of the AEJs to different levels of geomagnetic activity and seasonal variation. However, in their analysis they combined the results from the Northern and Southern Hemispheres, even though hemispheric differences are identifiable using their method.

In this paper, we apply the method of Vennerstrom and Moretto (2013) to the Swarm data set and to older satellite missions: Magsat and the POGO missions (OGO 2, OGO 4, and OGO 6), as well as the full reprocessed CHAMP data set. We examine the response to IMF clock angle and season, identifying hemispheric differences. By comparing results from each mission, we attempt to identify long-term variations which could be

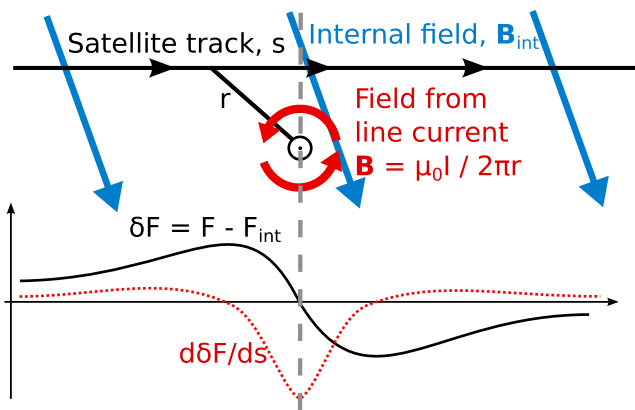


Figure 1. Summary of detection scheme. An internal field model is subtracted from the observed scalar field, $\delta F = F - F_{\text{int}}$. The electrojet contribution then has the demonstrated characteristic signature, with a maximum in $\frac{d\delta F}{ds}$ near the electrojet latitude. This maximum (either negative or positive) over each auroral region pass is picked as the electrojet latitude, and the magnitude of the maximum is used to estimate the electrojet current modeled as an infinite line current placed at that latitude.

an internal field model, F_{int} , must be subtracted: $\delta F = F - F_{\text{int}}$; that is, we isolate the ionospheric field from the core and crustal fields. As will now be discussed, we use the along-track gradient of F near the poles, to which the large-scale magnetospheric field has only a minimal contribution, so it is not necessary to subtract a model of this field.

As illustrated in Figure 1, the electrojet can be modeled as a single horizontal line current perpendicular to the satellite track (aligning approximately with the contours of magnetic latitude along which the currents flow since the satellite motion is north-south). Due to the motion of the satellite, the time derivative of δF , $\frac{d\delta F}{dt}$, is equivalent to the along-track gradient, $\frac{d\delta F}{ds}$, where ds is the distance traveled by the satellite during time dt . By assuming the electrojet remains static during a satellite pass, the peak in $\frac{d\delta F}{ds}$ therefore indicates the latitudinal location of the current, with its sign depending on the direction of the current. The size of the peak is used to calculate the strength of an equivalent infinite line current placed perpendicular to the satellite track at a height of 110 km (the peak of conductivity in the ionospheric E layer). We additionally include a small correction which accounts for the inclination of the main field away from the vertical, shifting the location of the peak (see Vennerstrom & Moretto, 2013).

It is important to note that the current estimated in this way really indicates the location of peak intensity, and more accurately represents the true current when the flow is concentrated in a narrow range of latitude compared to when the current system is more complicated. The real magnetic signature is wider than that produced from an infinite line current, so this will underestimate the true current. There can also be false positives and ambiguous situations when the magnetic signature does not conform to the idealized “single line current” form (e.g., when there is more than one large peak in $\frac{d\delta F}{ds}$, indicating multiple currents at different latitudes), leading to a wide range of latitude and current estimates. To screen out other nonelectrojet contributions at very low current strengths, electrojet detections are only accepted above a minimum threshold of 10 kA for CHAMP and Swarm measurements, consistent with Vennerstrom and Moretto (2013). A given detection alone does not represent the full complexity of the electrojet, but the method is sufficient to indicate the activity statistically under different conditions when large numbers of detections are considered.

Examples of detections are shown in Figure 2 for four passes from different satellite missions. In each case we show an ascending pass over the Northern Hemisphere, from 50° quasi-dipole latitude (QDLAT) toward the pole. Smoothing is applied to $\frac{d\delta F}{ds}$ as described in the following section. As already mentioned, the peak in $\frac{d\delta F}{ds}$ may be negative or positive depending on the direction of the current. For the analysis in this paper, we do not distinguish between eastward and westward currents and only use the current magnitude. Vennerstrom and Moretto (2013) demonstrated that this electrojet estimate tracks well over consecutive orbits, showing latitudinal expansion and contraction patterns associated with strengthening and weakening current strength during geomagnetic activity and a good correlation with the AE index.

attributed to secular variation of the core field. As already noted, these patterns have implications for internal field modeling (Finlay et al. 2017).

2. Method

The procedure we have adopted from Vennerstrom and Moretto (2013) is outlined here. Following the previous approaches (Moretto et al. 2002; Olsen, 1996), we use just the scalar magnetic field data, $F = |\mathbf{B}|$, rather than the full vector field, \mathbf{B} . The total magnetic field at a point combines internal and external sources (perturbations), $\mathbf{B} = \mathbf{B}_{\text{int}} + \mathbf{B}_{\text{ext}}$, with $\mathbf{B}_{\text{int}} \sim 40,000$ nT and $\mathbf{B}_{\text{ext}} \sim 100$ nT at altitudes of satellites in low Earth orbit when above 50° latitude, as in this study. This means that by separating the total field, \mathbf{B} , into components parallel (\mathbf{B}_{\parallel}) and perpendicular (\mathbf{B}_{\perp}) to the internal field, we get $\mathbf{B}_{\perp} \ll \mathbf{B}_{\parallel}$, and so \mathbf{B}_{\parallel} can be approximated by the magnetic field total intensity (scalar), F :

$$F = |\mathbf{B}| = \left(\mathbf{B}_{\parallel}^2 + \mathbf{B}_{\perp}^2 \right)^{\frac{1}{2}} = |\mathbf{B}_{\parallel}| \left(1 + O(10^{-5}) \right)^{\frac{1}{2}} \quad (1)$$

This means that perturbations to the parallel field component can be observed from the scalar measurements, F . Of the two main perturbing fields, that produced by the electrojet and that produced by the FAC, the FAC field effect on F is much smaller as it acts perpendicular to \mathbf{B} . Perturbations to F are therefore due primarily to the electrojet. To isolate this perturbation, δF ,

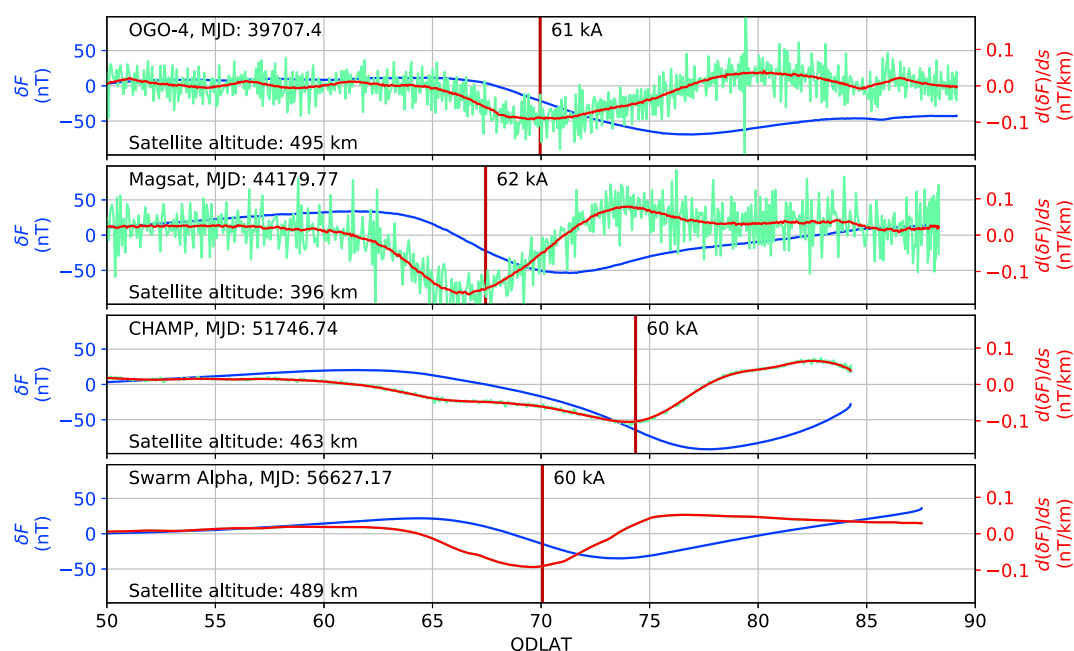


Figure 2. Examples of detections from OGO 4, Magsat, CHAMP, and Swarm Alpha. The blue line shows δF , the measured scalar field residual to the internal field model. The green line shows $\frac{d\delta F}{ds}$, and the red line shows it smoothed, except for Swarm where smoothing is not applied. The vertical line marks the determined electrojet latitude, and the estimated current strength is indicated.

The data are segregated into passes over the northern and southern auroral regions, $>|50^\circ|$ QDLAT, and further into the ascending and descending phases (toward and away from the pole), and so up to four electrojet signals can be detected on each orbit. A problem arises due to the offset of the geographic axis (the orbital convergence region) from the magnetic poles (the center of the auroral oval) and the polar gap in coverage, leading to incomplete and biased sampling of the electrojets. To help preserve the true oval shape within the collected detections (see Figure 3), a criterion is employed that essentially excludes the region between the geographic and magnetic poles, that is, the polar passes are split (into the ascending and descending phases) such that we exclude the section of the polar pass between the orbit's maxima in geographic (GLAT) and magnetic latitudes (QDLAT). The ascending phase begins at 50° QDLAT and ends at the maximum of GLAT or QDLAT, whichever the satellite arrives at first. The descending phase begins where both GLAT and QDLAT are decreasing again and ends at 50° QDLAT.

3. Data

To adequately sample the AEJs, low-altitude ($\lesssim 600$ km) polar-orbiting magnetic satellite data are required. This requirement is satisfied by the POGO missions, OGO 2, OGO 4, and OGO 6 (over part of their orbits), Magsat, CHAMP, and Swarm. OGO 2 operated from October 1965 to September 1967 at 413–1,510 km altitude, OGO 4 from July 1967 to January 1969 at 412–908 km, and OGO 6 from June 1969 to July 1971 at 397–1,098 km, each providing data at all local times. For POGO data, we use only those when the satellites are below 600 km. OGO 2 is in a more elliptical orbit so it only contributes a relatively small amount of useful data. Magsat operated from November 1979 to May 1980 in a dawn/dusk orbit at 325–550 km and CHAMP from July 2000 to September 2010 at 454–270 km. Swarm launched in November 2013 and is a trio of satellites: after the 3 month commissioning phase Alpha and Charlie flew side by side at ~ 450 km altitude, and Bravo at ~ 530 km; they have increasing local time separation. We therefore use data from Alpha and Bravo (since Charlie detects the same electrojet signal as Alpha with our method) up until the end of 2014 to match the end point of the internal field model used.

In each case, we use 1 Hz scalar data sets where available or resample the original data to 1 Hz. We then apply a smoothing using a running average over a window of 30 s to filter out high frequency noise, except in the case of Swarm where the data are of high enough quality that this is not necessary. CHAMP data are from the Level 3 reprocessed set, and Swarm data are from version 0408 of the Level1b MAGx_LR set.

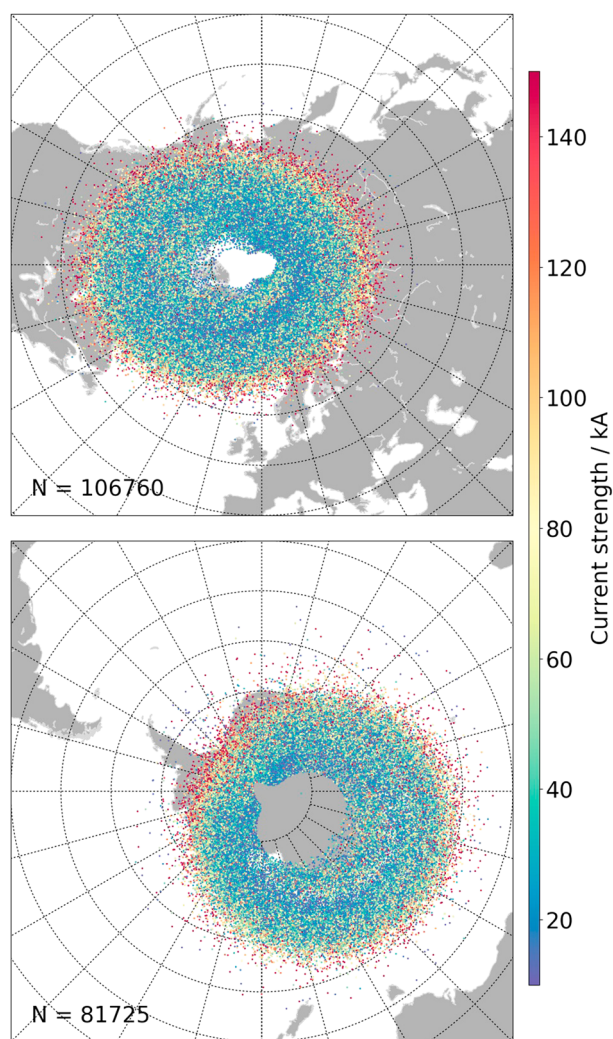


Figure 3. All detections collected from the CHAMP and Swarm-2014 data, colored by inferred current strength. (top) The Northern and (bottom) Southern Hemispheres; the graticule is segmented by 10° in geographic latitude and 15° in longitude. The total number of detections, N , is indicated.

the geographic poles produces a longitudinal bias in the number of detections, which is not significant in the north but is in the south due to the greater offset. However, the effect of the longitudinal bias is reduced when we consider activity as a function of MLT. The greater offset in the south also leads to a greater loss of detections over the polar gap. This contributes to a lower number of detections overall in the south and a bias toward lower latitudes (which would typically be of higher current strength). The lower number of detections could also be partly due to hemispheric asymmetries in the current strengths and fewer detections due to the current detection threshold (i.e., very small currents are ignored). These issues make it difficult to directly compare the average current strengths and positions between hemispheres, but comparisons between different MLT sectors in the same hemisphere are not strongly affected.

Figures 4 and 5 show the response of the AEJs as a function of MLT, separately for each hemisphere for different IMF directions and different seasons, for CHAMP and Swarm-2014 data. We use the hour-averaged IMF direction at the time of each detection, with direction split into four quadrants according to the sign of B_z and B_y . We denote $B_z > 0$ as B_z^+ , $B_z < 0$ as B_z^- , and the same for B_y . The detections are collected in bins of 1 h MLT and for each MLT sector, the mean and standard deviation of QDLAT are indicated by the oval position and half width, and the mean current strength is indicated by the color. Well-known features are produced: stronger substorm- and convection-associated currents on the nightside; high-latitude cusp currents on the

To isolate the ionospheric field from the measured magnetic field, we must subtract the contribution from the core and the crust using a consistent field model for each date period studied. For this we use a combination of the COV-OBSx1 core field model (Gillet et al. 2015) up to degree 14 (which spans years 1940.0 to 2015.0) and a static contribution from degrees 15–110 of CHAOS-6 (Finlay et al. 2016), respectively.

Values for the AE and Kp indices and the IMF conditions are drawn from the hour-averaged and minute NASA OMNI 2 databases which draw data together from a number of sources, with solar wind conditions time shifted to the magnetosphere bow shock. The SuperMAG auroral electrojet index (SME) which we use was obtained on 18 April 2017 and is produced from many ground stations (Gjerloev, 2012).

We also make use of the quasi-dipole (QD) coordinate system which is the most appropriate for organizing ionospheric currents (Laundal & Richmond, 2017). We refer to QD latitude as QDLAT and magnetic local time (calculated from QD longitude and the subsolar point) as MLT. To calculate QD coordinates, we use a Python library, *apexpy*, based on Emmert et al. (2010).

4. Results

4.1. CHAMP and Swarm: Response to IMF Direction, Season, and Solar Cycle

Figure 3 shows the collection of all detections from CHAMP and Swarm Alpha and Bravo together (using just the data from 2014 for compatibility with the COV-OBS model). Familiar features can already be seen. The auroral ovals are centered around the magnetic poles, with a more elliptical form in the Northern Hemisphere following the horizontal intensity contours of the main magnetic field. Lower latitude signals tend to have stronger current strengths, and a higher latitude inner ring can be seen separate from the main oval which corresponds to detections on the dayside due to cusp currents. We initially used only a core field model subtraction, but in that case we observed clustering of detections around known crustal magnetic features, motivating the inclusion of a high degree crustal field model which resolved this issue. There still may be small issues of crustal field contamination, particularly in the south where the crustal field is less well known, but the results are not strongly dependent on the particular core and crustal field models chosen.

Orbital effects produce uneven sampling. Orbital convergence produces a higher density of detections close to the poles. The offset of the magnetic poles from

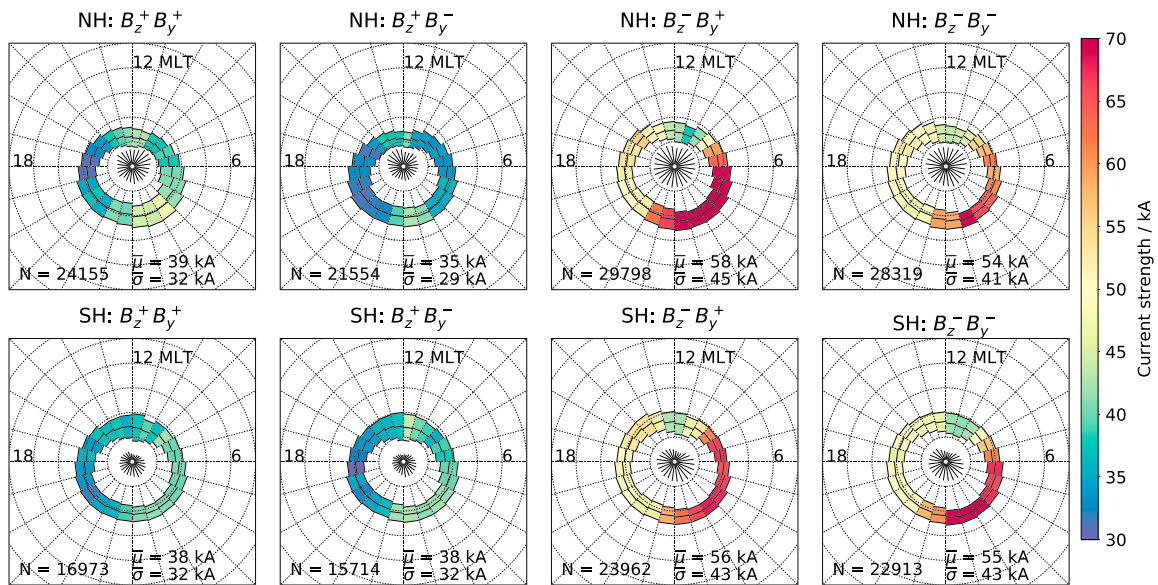


Figure 4. Collected detections from CHAMP and Swarm-2014 data in bins of 1 h MLT. The latitudinal position and half width of each bin mark the mean and standard deviation of QDLAT, and the color indicates the mean current strength. Data are split by hemisphere and by IMF direction. NH, Northern Hemisphere; SH, Southern Hemisphere; B_z^{\pm}/B_y^{\pm} : $B_z > 0 / B_z < 0$, etc. The mean current strength, $\bar{\mu}$, and mean of the standard deviations of current strengths in each bin, $\bar{\sigma}$, are indicated. The graticule is spaced by 10° in QDLAT. The numbers of detections in each bin are indicated by the lengths of the lines in the center and are between 766 and 1,371 in the NH and between 383 and 1,302 in the SH.

dayside; stronger response during southward IMF (B_z^-); stronger response around the equinoxes due to the Russell-McPherron effect (Russell & McPherron, 1973); and stronger response during local summer compared to winter due to increased conductivity and cusp currents (particularly on the dayside).

In Figure 4, all seasons are considered together so the seasonal effects are not visible. Mean dayside currents are between 35 kA and 45 kA and do not vary much between different IMF directions. The dawn currents are stronger than the dusk currents in all cases. Both dawn and dusk currents are strongly increased by southward IMF (B_z^-), increasing from 30–45 kA (B_z^+) to 50–70 kA (B_z^-). The nightside currents are yet more strongly affected, increasing from 35–50 kA to 60–70+ kA.

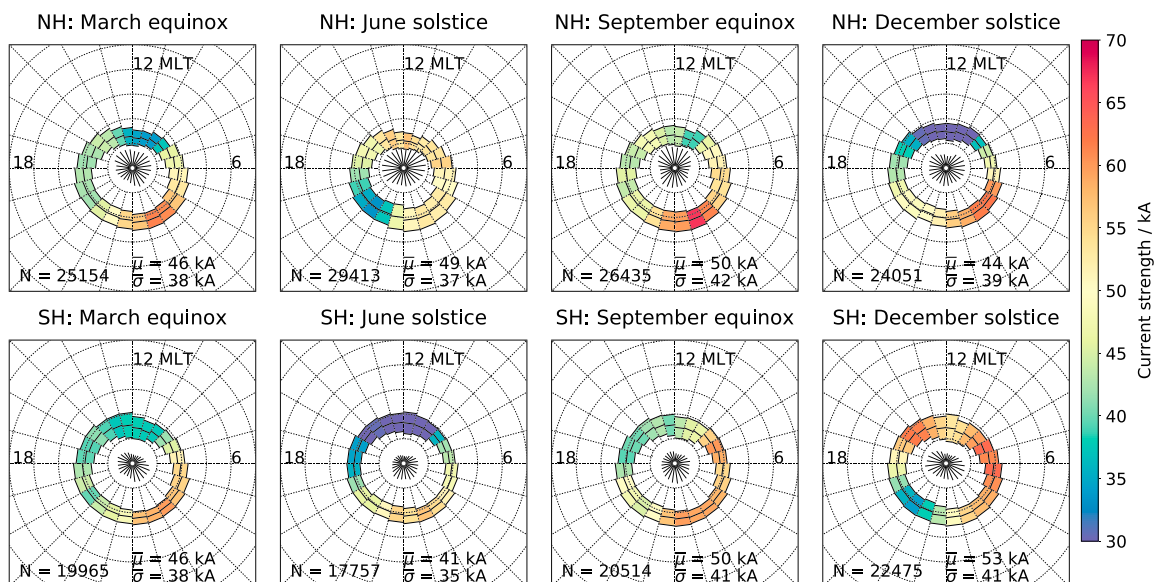


Figure 5. As for Figure 4, but data are instead split according to season. Each season selection is composed from data taken 45 days each side of each solstice/equinox. The number of detections in each bin is between 755 and 1,476 in the NH and between 411 and 1,202 in the SH.

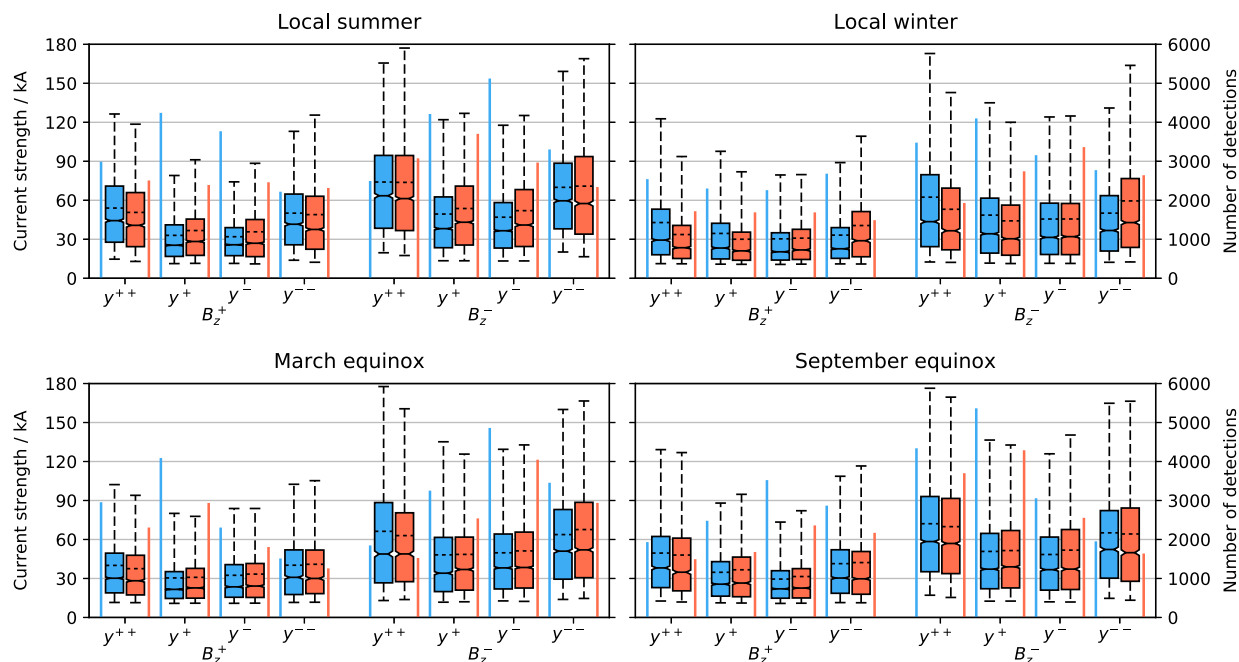


Figure 6. Box plots of current strengths from all detections around the full oval in MLT, from all the CHAMP and Swarm-2014 data, split according to hemisphere, season, and IMF direction. Local summer/winter means 45 days either side of the June/December solstice, depending on hemisphere. In each season, IMF conditions are split between $B_z > 0$ (indicated by B_z^+) and $B_z < 0$ (B_z^-) and further divided by $B_y > 3$ nT (y^{++}), $0 < B_y < 3$ nT (y^+), -3 nT $< B_y < 0$ (y^-), and $B_y < -3$ nT (y^{--}). The Northern Hemisphere measures take blue boxes, and the Southern Hemisphere red boxes. For each box, the median current strength is indicated by the solid line with notches, the mean by the dashed line, the 25th and 75th percentiles by the boundaries of the solid box, and the 5th and 95th percentiles by the vertical whiskers. The number of detections contributing to each is indicated by the vertical line beside each box.

There are also differences in the response to the sign of B_y . For the Northern Hemisphere during B_z^+ , the dayside, dawn, and nightside currents are slightly stronger for B_y^+ than for B_y^- , with an increase of the mean current around the full oval from 35 kA to 39 kA; during B_z^- , the dawn, dusk, and nightside currents are stronger for B_y^+ , with an increase of the mean current from 54 kA to 58 kA. Conversely, in the Southern Hemisphere, for B_z^+ or B_z^- , the current strengths are more similar for each sign of B_y .

In Figure 5, all IMF directions are considered together, so we can only see the seasonal variations. The mean dayside currents are most strongly affected, varying from 30 kA in winter to 55 kA in summer, for both hemispheres. The peak in current strength during local summer is around 12 MLT for the Northern Hemisphere. For the Southern Hemisphere, however, there are two peaks, one in the afternoon sector and one around dawn, where the mean current strength increases to 60 kA. This gives rise to a larger overall mean current strength of 53 kA in the southern summer compared to 49 kA in the northern summer. As in Figure 4, dawn currents are stronger than dusk currents and are not so strongly affected by season as the dayside currents. Outside of local summer, similar nightside current strengths are observed, which are slightly stronger than during summer and slightly stronger for the Northern Hemisphere than the Southern Hemisphere.

Figure 6 compares the current strengths from the full oval for each hemisphere for both varying IMF direction and season. This separates the effects of IMF direction and season, since we expect the effect of IMF direction to be season dependent. Response to IMF is split according to the sign of B_z , and each further split according to the sign of B_y and its magnitude, $|B_y| < 3$ nT or $|B_y| > 3$ nT. Box plots show the distribution of current strengths in each bin. The number of samples in each is also indicated and ranges from 1,225 to 5,331, typically being lower in the Southern Hemisphere (SH). In all seasons, currents are stronger for $B_z < 0$, and stronger for $|B_y| > 3$ nT than $|B_y| < 3$ nT, indicating the increased magnetopause reconnection for southward IMF and for IMF of greater magnitude. Current strengths in summer tend to be higher in the SH than the Northern Hemisphere (NH) for $|B_y| < 3$ nT, for both signs of B_z but are more similar in each hemisphere for $|B_y| > 3$ nT, which indicates the increased role of insolation rather than IMF driving hemispheric asymmetry during summer. In winter, increasing magnitude of B_y shows an asymmetry in the hemispheric response: currents are stronger

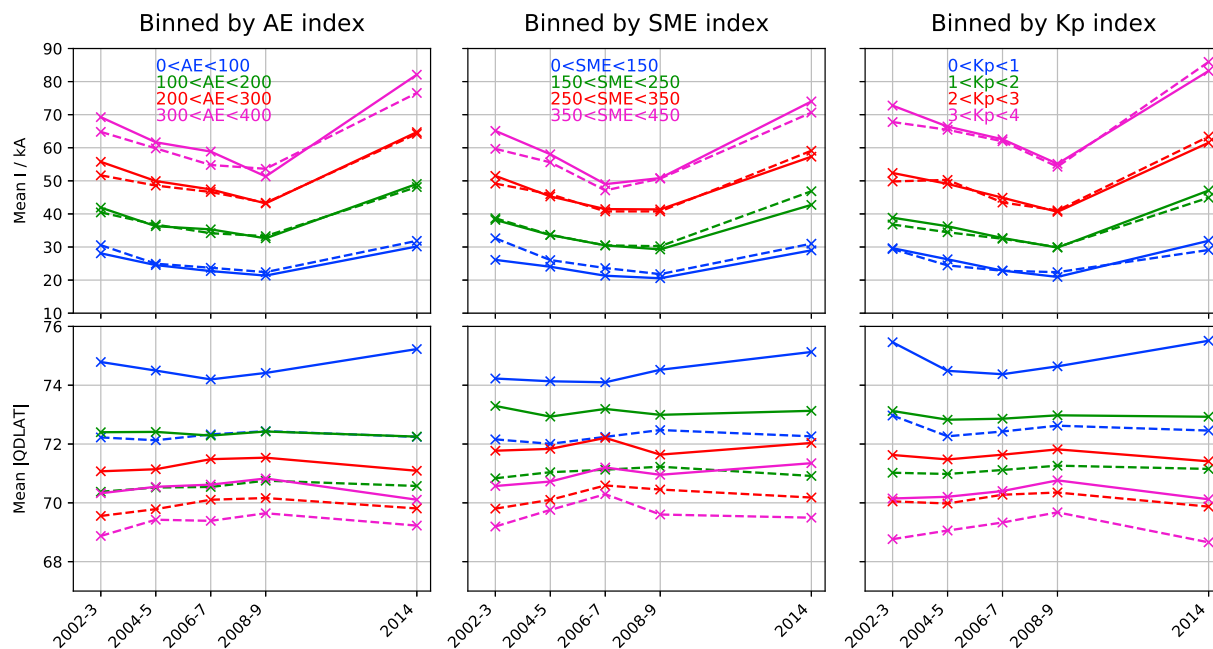


Figure 7. Mean current strengths for the full oval split according to the AE, SME, and Kp indices at the time of each detection and split into consecutive 2 year periods from CHAMP and for just 2014 from Swarm. Solid line: Northern Hemisphere, dashed line: Southern Hemisphere. The effect of the solar cycle (decreasing activity from 2002 to 2010 and increased again at 2014) is visible, even after grouping the data into similar levels of geomagnetic activity as determined by ground-based measurements.

in the NH for $B_y > 0$ than for $B_y < 0$ but stronger in the SH for $B_y < 0$ than for $B_y > 0$, for both signs of B_z , with an increasing disparity at $|B_y| > 3$ nT. This effect is unclear around the equinoxes and during summer.

Figure 7 shows the mean current strength and QDLAT in each hemisphere from consecutive 2 year periods. By combining data from 2 years, MLT and seasonal variation are similarly sampled between each 2 year period, smoothing out the effect of the variable solar wind geoeffectiveness that a particular individual year carries. Data are split according to the AE (1 min), SME (1 min), and Kp (3 h) indices at the time of each detection. The mean latitudes for the Southern Hemisphere are lower than the Northern Hemisphere due to the bias in the detections arising from the greater polar gap. Selecting SH data from only the geographic longitude sector which is most accurately sampled ($\sim 105^\circ - 160^\circ$) reveals that this is the case, with very similar mean |QDLAT| as the NH measure (not shown here). For all three indices, there is the expected shift to higher current strengths for higher activity levels but also a trend which corresponds to the solar cycle maximum around 2002, minimum around 2008, and increasing again at 2014. For the mean latitude, there appears to be similar but more complicated trends related to the solar cycle. In each case, for the two higher activity levels, there is a trend to higher latitudes at the solar minimum, while the trend is reversed for the lowest activity level selection. The solar cycle trend has implications for main field modeling and also demonstrates the issue of variation associated with the solar cycle (or even longer-term trends in solar activity) facing measurement of secular variation of the AEJs.

4.2. Secular Variation of the Oval

As we have seen, there are several variations in the AEJs associated with different physical drivers: MLT and seasonal responses due to Earth's rotation and orientation (affecting both insolation-driven conductivity and solar wind-magnetosphere coupling); main field morphology and hemispheric asymmetries; and responses to solar wind conditions and the solar cycle. This makes it challenging to observe long-term variation in the electrojets. We expect that such variation would be in the form of a shift in position of the oval due to shift of the magnetic poles (and more subtle change in the morphology) and change in intensity (and latitudinal extent) due to variation both in the main field dipole strength (and so the amount of solar wind energy entry) and in long-term trends in solar activity.

In Figure 8 we attempt to identify variation in the electrojet position due to the main field secular variation over the period 1970–2015. Electrojet position estimates are made from seven satellites: collectively OGO 2,

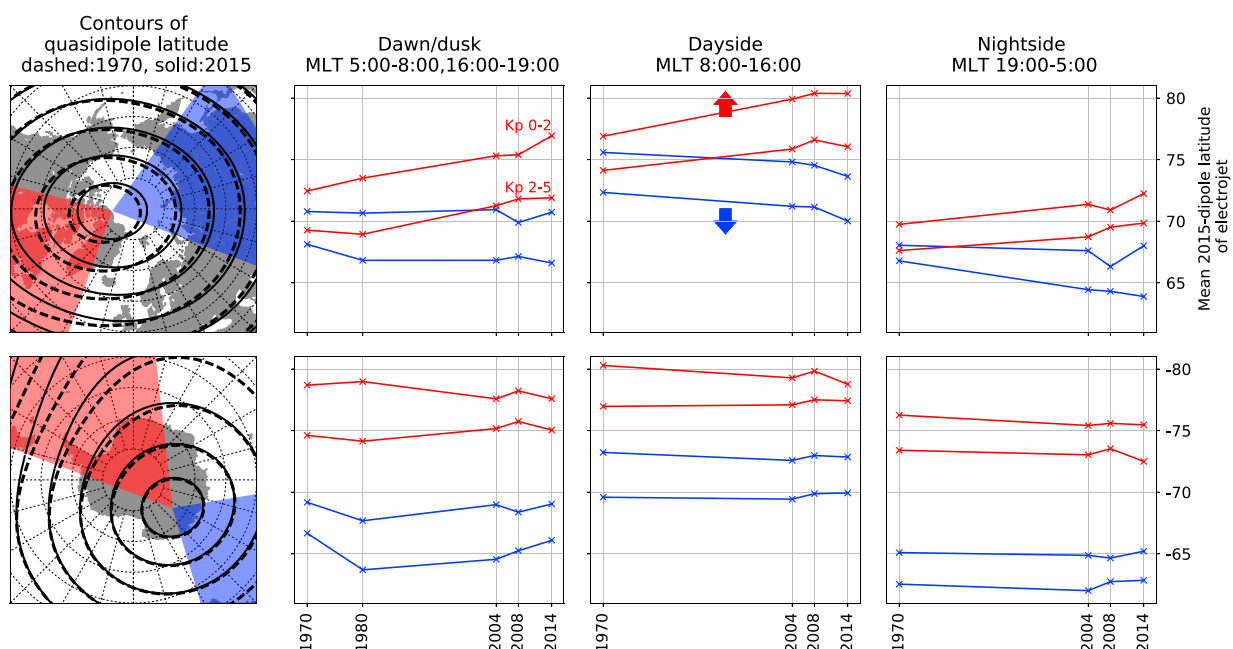


Figure 8. (first column) Contours of QDLAT for 1970 and 2015 over each hemisphere, with divisions into two sectors of differing change (shifting to either higher or lower latitudes) colored red and blue. (second to fourth columns) (top, Northern Hemisphere; bottom, Southern Hemisphere): Each shows the latitudinal responses of the AEJs in different MLT sectors. Mean latitudes of all detections are compared from OGO 2, OGO 4, and OGO 6 (combined into one period marked 1970), Magsat (marked 1980), CHAMP (split 2002–2005 and 2006–2009), and Swarm (2014). Data are split into the two sectors marked in the maps (the red and blue coloring of lines indicate which sector they refer to). Responses during low K_p (0–2) and high K_p (2–5) are shown. The arrows indicate the poleward shift of the AEJs in the Northern Hemisphere sector colored red (red lines) and the equatorward shift for the sector colored blue (blue lines).

OGO 4, and OGO 6 (~1967–1971); Magsat (~1980); CHAMP (2002–2009); and Swarm Alpha and Bravo (2014). The results derived from POGO and Magsat data, with plots analogous to Figures 3 to 5, can be found in the supporting information. We select two sectors from each pole (colored red and blue), according to the differing main field variation in each sector as seen by the shift in contours of QDLAT, in order to compare latitudinal variation of the electrojets in each sector separately. We further split by MLT, roughly corresponding to electrojets with different origins: dawn/dusk convection, dayside cusp currents, nightside convection, and substorms. Mean latitudes are compared for low and high K_p index. The reason for this separation by MLT and K_p index is to attempt to account for variation of solar wind forcing, so that remaining trends are isolated from this. For each satellite, we show the mean dipole latitudes (fixed to the 2015 dipole) of the electrojets detected in each sector.

The data points for 1970 and 1980 are both close to solar maxima, whereas the data points for 2004 and 2008 are for periods moving away from solar maximum (around 2000/2001), and 2014 is again solar maximum (albeit an atypically weak maximum). Due to increased activity near solar maxima, we would expect AEJs at lower latitudes at these times, which holds true more for during $K_p > 2$, as in Figure 7. There is not a consistent trend in the data points to this effect, so we do not believe solar cycle effects are strongly influencing these results.

Although the earlier data are very noisy and there are many complicating factors (the highly variable nature of the AEJs, varying data quality, and varying biases introduced by the satellites' orbits), expected patterns are reproduced: dayside electrojets are at higher latitudes; nightside electrojets (which include substorms) are at lower latitudes; dawn/dusk electrojets are at intermediary latitudes; and higher levels of the K_p index show lower-latitude electrojets. In the Northern Hemisphere sector colored red we see the largest variation in QDLAT, with a shift to higher latitudes over time from 1970 to 2015. The Northern Hemisphere sector colored blue has a slightly smaller shift but to lower latitudes over time. Although certainly not conclusive, there are corresponding trends in the measured electrojet positions for these sectors for all three MLT sectors, while the sectors in the south are more constant.

4.3. Discussion

The results presented are consistent with the previous results of Vennerstrom and Moretto (2013): the AEJs increase in intensity and extend equatorward with increasing geomagnetic activity, are typically stronger in the dawn sector with a weaker peak in the afternoon sector, and are stronger on the dayside during local summer. However, with the application to more data and separation by hemisphere, we have shown that there are subtle asymmetries in the way in which the AEJs in each hemisphere respond to solar wind and seasonal drivers, as well as the longer-term asymmetry associated with core field change which is hidden by the use of QD coordinates.

The seasonal changes in the MLT patterns compare favorably with recent studies of the FACs (e.g., Laundal, Finlay, et al., 2016), driven by the variations in sunlight and particle precipitation. In winter, currents are stronger on the nightside and weaker on the dayside; in summer the dayside currents are stronger. The dusk sector has stronger currents in the winter than in the summer, which is consistent with stronger/weaker FACs here measured by Laundal, Finlay, et al. (2016), who attribute this to suppression of auroral precipitation in sunlight (Newell et al. 2010). The same effect should also cause stronger dawn currents in summer. However, we find stronger dawn currents in the winter for the NH between 0 and 6 MLT, while in the SH dawn currents are stronger in winter between 0 and 2 MLT but stronger in summer between 2 and 6 MLT. This may be due to increased effect of the substorm current in our measure, which is most noticeable during winter and the equinoxes, while the SH may be more insolation-driven in the summer than the NH is.

Laundal, Finlay, et al. (2016) also measured the horizontal equivalent currents, finding that the overall summertime currents are stronger in the south than in the north (during conditions of $B_z < -1$ nT) by 6% and that this is reversed in winter with stronger currents in the north than the south by 16%. We find the same asymmetry, with hemispheric differences of 8% and 7% in summer and winter, respectively. Differences in the values arise because the measures are very different: measurements of the full current distribution over the whole polar region versus an average of the individual AEJ estimates made at different positions and times. This is in contrast with studies using the AMPERE data set (e.g., Coxon et al., 2016) in which the summer FACs are significantly stronger for the Northern Hemisphere. This may be due to poorer AMPERE data quality since it is derived from magnetometers of much lower sensitivity.

The disparity between mean current strengths in summer compared to winter is greater in the SH than in the NH (29% summer/winter difference in the SH compared to 11% in the NH), with a different MLT pattern in intensity, and not strongly related to IMF direction. We suggest that this may be a result of the different insolation pattern over the southern oval due to the increased geographic offset of the southern magnetic pole. The southern oval experiences longer periods with more sunlight than the northern but also periods with less sunlight (but these are shorter than the periods with more sunlight). There is also an increase in insolation around January due to perihelion, which is also a driver for stronger southern summer currents. However, there is a systematic bias toward stronger current strength measurements in the south due to the loss of higher-latitude detections (which are typically weaker) due to the polar gap in satellite coverage. Conversely, there is potentially a greater underestimation of the true current strength from each satellite pass in the south than the north because there is a greater deviation of the QDLAT contours from the perpendicular to the satellite track along which the model line current flows. Despite these issues, the comparison of current strengths between different conditions for the same hemisphere is quite robust due to the large number of detections considered in each case and because the conditions are unrelated to the sampling by the satellites.

We have been able to show seasonal tendencies because we have sufficient sampling from ~ 10 years of data which averages out contributions from the solar wind variation between individual seasons. The seasonal variations are further complicated by hemispheric differences in the reaction to solar wind conditions (and indeed in tendencies of the IMF toward particular orientations). We have explored the seasonal response, in each hemisphere, to the signs of the IMF B_z and B_y components. The observed increase in current strength for $B_y > 0$ in the Northern Hemisphere winter agrees with previous results from ground-based studies (Friis-Christensen et al., 2017; Friis-Christensen & Wilhjelm, 1975; Laundal, Gjerloev, et al., 2016). The asymmetric B_y response between hemispheres is likely to be associated, on the dayside and dawn/dusk, with modification of the polar convection cells (Tenfjord et al. 2015) and, on the nightside, with twisting of the magnetotail (Østgaard et al. 2016).

The solar cycle's appearance within the AEJs, even after grouping by similar levels of geomagnetic activity, demonstrates an issue in main field modeling: although geomagnetic activity may have been "accounted for"

by index-based data selection, there are likely still solar cycle trends in external-field noise within data used for modeling. This is confounded by the fact that more data will be used at solar minimum because there are more periods of low activity. The solar cycle trend appears in the satellite data when contrasting with the ground data (in the case presented, with the *AE*, *SME*, and *Kp* indices), indicating that satellite data contain trends not seen in ground data. We therefore suggest that the geomagnetic index-based data selection used in internal field modeling (Kauristie et al. 2017) may be enhanced by the use of a satellite-based index when selecting satellite data. The appearance of these trends in the along-track gradient in polar regions is particularly pertinent as it represents one of the largest noise sources in internal field modeling (Olsen & Stolle, 2017).

4.3.1. Application to Space Weather Hazards

The climatological behavior which we have shown is relevant to the development of improved geomagnetic activity indices monitoring the AEJs. The underlying quiet time trends in activity, whether through seasonal or solar cycle drivers, need to be accounted for. For a satellite-based activity index, these trends should be removed in order to be comparable to the existing ground-based indices which remove these trends by the monthly changing baseline. We have identified some of these trends, but further work is needed to properly quantify them. Such an index would be useful in conjunction with the ground-based indices and could be deployed in near-real time, subject to data down linking constraints, for space weather monitoring purposes.

The trends in the AEJ response to solar wind conditions, together with the seasonal and longer-term variations, will influence GICs and atmospheric heating. To assess this influence, an empirical model of the AEJs would be useful, which necessarily must include these trends and a more realistic current distribution than that presented here. By including these effects (long-term behavior and interhemispheric differences not visible in the traditional activity indices), better understanding may be reached about the cumulative effect that they have. For example, cumulative atmospheric heating influences satellite lifetime through increasing drag, and the real baseline will affect real-time predictions of drag. Likewise, GICs influence the lifetime of pipelines through increased corrosion.

The location and intensity of the AEJs indicate levels of radiation entering the ionospheric polar cap. With the increase in the number of polar flights, radiation effects on personnel and passengers need to be better quantified. High-latitude directional drilling is also affected by the AEJs due to reliance on magnetic navigation systems. Both of these could benefit from better baseline data of the AEJs.

We investigated the effect of IMF clock angle (B_z and B_y), as the largest driver of change, but not other solar wind parameters. To more fully parameterize the driving of the AEJs, time-of-year and solar wind coupling functions could be used along with appropriate MLT-dependent time averaging to account for the solar wind time history and the different magnetospheric unloading processes. The ongoing Swarm mission will be invaluable in providing data for this purpose.

5. Summary

By tracking peaks in the along-track field intensity gradient over each auroral region satellite pass, after subtracting an internal field model, we have obtained practical estimates of the AEJ strength and location and have demonstrated the utility of this approach for studying their behavior in response to a number of drivers. We have used it to show broadly the response of the system to drivers from IMF direction and season, within the context of hemispherical differences due to the core field asymmetry, using the high-quality data provided by CHAMP and Swarm (with reasonable results obtainable from Swarm data without smoothing).

We found that during local winter, AEJ currents are, on average, stronger in the Northern Hemisphere than in the Southern Hemisphere for IMF $B_y > 0$ and stronger in the Southern Hemisphere for $B_y < 0$. This asymmetry tends to disappear during summer, and instead we see stronger average currents in the south regardless of IMF direction. We attribute this partly to the increased role of insolation during summer and the different southern auroral oval insolation pattern due to the greater southern geomagnetic pole offset. We have also compared results with older satellites, POGO and Magsat, to show the AEJ response to secular variation of the core field and validity of QD coordinates for controlling the morphology the AEJs.

We highlighted the issue of separating the ionospheric field from the core and crustal fields, finding that it was essential to remove the crustal field to obtain reasonable results from our method. This is indicative of the mutual contamination of magnetic field measurements from the crust and from the ionosphere, which often

have similar magnitudes and scale lengths when measured from LEO satellites. We also demonstrated some of the solar cycle-related trends that presumably contaminate internal field models of the secular variation in as yet unknown ways and that should be considered for the development of AEJ activity indices or models.

Acknowledgments

We are grateful to Nils Olsen and Christopher Finlay at DTU Space for the suggestion to use and for providing access to POGO data, and for help with combining the COVOBS and CHAOS models. We are also very grateful to two anonymous reviewers who provided detailed feedback on the manuscript. We would also like to thank the many institutes around the world involved in operating observatories and variometer stations, whose data are used to produce magnetic activity indices, and to those building and supporting the satellite missions. CHAMP Level 3 data are available at ftp://magftp.gfz-potsdam.de/CHAMP/L3_DATA. Swarm data are available after registration at <https://earth.esa.int/web/guest/swarm/data-access>. POGO and Magsat data are available at <ftp://ftp.space.dtu.dk/data/magnetic-satellites>. The OMNI data are available through the NASA GSFC SPDF at <https://omniweb.gsfc.nasa.gov>. The SuperMAG data are available at <http://supermag.jhuapl.edu>. The COVOBS and CHAOS models are available at http://www.space.dtu.dk/english/Research/Scientific_data_and_models/Magnetic_Field_Models. A. R. A. S. is funded through the E3 DTP at the University of Edinburgh by NERC grant NE/L002558/1, and a NERC CASE studentship with a British Geological Survey BUFI grant (BGS contract GA/15S/006).

References

- Aakjær, C. D., Olsen, N., & Finlay, C. C. (2016). Determining polar ionospheric electrojet currents from Swarm satellite constellation magnetic data. *Earth, Planets and Space*, *68*(1), 140. <https://doi.org/10.1186/s40623-016-0509-y>
- Browett, S. D., Fear, R. C., Grocott, A., & Milan, S. E. (2017). Timescales for the penetration of IMF B_y into the Earth's magnetotail. *Journal of Geophysical Research: Space Physics*, *122*, 579–593. <https://doi.org/10.1002/2016JA023198>
- Cnossen, I. (2017). The impact of century-scale changes in the core magnetic field on external magnetic field contributions. *Space Science Reviews*, *206*, 259–280. <https://doi.org/10.1007/s11214-016-0276-x>
- Coxon, J. C., Milan, S. E., Carter, J. A., Clausen, L. B. N., & Korth, H. (2016). Seasonal and diurnal variations in AMPERE observations of the Birkeland currents compared to modelled results. *Journal of Geophysical Research: Space Physics*, *121*, 4027–4040. <https://doi.org/10.1002/2015JA022050>
- Davis, T., & Sugiura, M. (1966). Auroral electrojet activity index AE and its universal time variations. *Journal of Geophysical Research*, *71*(3), 785–801. <https://doi.org/10.1029/JZ071i003p00785>
- Dungey, J. W. (1961). Interplanetary magnetic field and the auroral zones. *Physical Review Letters*, *6*(2), 47–48. <https://doi.org/10.1103/PhysRevLett.6.47>
- Emmert, J. T., Richmond, A. D., & Drob, D. P. (2010). A computationally compact representation of magnetic-apex and quasi-dipole coordinates with smooth base vectors. *Journal of Geophysical Research*, *115*, A08322. <https://doi.org/10.1029/2010JA015326>
- Finch, I., & Lockwood, M. (2007). Solar wind-magnetosphere coupling functions on timescales of 1 day to 1 year. *Annales Geophysicae*, *25*(2), 495–506. <https://doi.org/10.5194/angeo-25-495-2007>
- Finlay, C. C., Olsen, N., Kotsiaros, S., Gillet, N., & Clausen, L. T. (2016). Recent geomagnetic secular variation from Swarm and ground observatories as estimated in the CHAOS-6 geomagnetic field model. *Earth, Planets and Space*, *68*, 112. <https://doi.org/10.1186/s40623-016-0486-1>
- Finlay, C. C., Lesur, V., Thébault, E., Vervelidou, F., Morschhauser, A., & Shore, R. (2017). Challenges handling magnetospheric and ionospheric signals in internal geomagnetic field modelling. *Space Science Reviews*, *206*, 157–189. <https://doi.org/10.1007/s11214-016-0285-9>
- Friis-Christensen, E., & Wilhelm, J. (1975). Polar cap currents for different directions of the interplanetary magnetic field in the Y - Z plane. *Journal of Geophysical Research*, *80*(10), 1248–1260. <https://doi.org/10.1029/JA080i010p01248>
- Friis-Christensen, E., Finlay, C. C., Hesse, M., & Laundal, K. M. (2017). Magnetic field perturbations from currents in the dark polar regions during quiet geomagnetic conditions. *Space Science Reviews*, *206*(1–4), 281–297. <https://doi.org/10.1007/s11214-017-0332-1>
- Gaunt, C. T. (2016). Why space weather is relevant to electrical power systems. *Space Weather*, *14*(1), 2–9. <https://doi.org/10.1002/2015SW001306>
- Gillet, N., Barrois, O., & Finlay, C. C. (2015). Stochastic forecasting of the geomagnetic field from the COV-OBS.X1 geomagnetic field model, and candidate models for IGRF-12. *Earth, Planets and Space*, *67*(1), 71. <https://doi.org/10.1186/s40623-015-0225-z>
- Gjerloev, J. W. (2012). The SuperMAG data processing technique. *Journal of Geophysical Research*, *117*, A09213. <https://doi.org/10.1029/2012JA017683>
- Juusola, L., Kauristie, K., Amm, O., & Ritter, P. (2009). Statistical dependence of auroral ionospheric currents on solar wind and geomagnetic parameters from 5 years of CHAMP satellite data. *Annales Geophysicae*, *27*(3), 1005–1017. <https://doi.org/10.5194/angeo-27-1005-2009>
- Kauristie, K., Morschhauser, A., Olsen, N., Finlay, C. C., McPherron, R. L., Gjerloev, J. W., & Opgenoorth, H. J. (2017). On the usage of geomagnetic indices for data selection in internal field modelling. *Space Science Reviews*, *206*, 61–90. <https://doi.org/10.1007/s11214-016-0301-0>
- Laundal, K. M., & Richmond, A. D. (2017). Magnetic coordinate systems. *Space Science Reviews*, *206*(1), 27–59. <https://doi.org/10.1007/s11214-016-0275-y>
- Laundal, K. M., Finlay, C. C., & Olsen, N. (2016). Sunlight effects on the 3D polar current system determined from low Earth orbit measurements. *Earth, Planets and Space*, *68*(1), 142. <https://doi.org/10.1186/s40623-016-0518-x>
- Laundal, K. M., Gjerloev, J. W., Østgaard, N., Reistad, J. P., Haaland, S., Snekvik, K., ... Milan, S. E. (2016). The impact of sunlight on high-latitude equivalent currents. *Journal of Geophysical Research: Space Physics*, *121*, 2715–2726. <https://doi.org/10.1002/2015JA022236>
- Laundal, K. M., Cnossen, I., Milan, S. E., Haaland, S. E., Coxon, J., Pedatella, N. M., ... Reistad, J. P. (2017). North-south asymmetries in Earth's magnetic field. *Space Science Reviews*, *206*(1), 225–257. <https://doi.org/10.1007/s11214-016-0273-0>
- Lockwood, M., Owens, M. J., Barnard, L. A., Bentley, S., Scott, C. J., & Watt, C. E. (2016). On the origins and timescales of geoeffective IMF. *Space Weather*, *14*, 406–432. <https://doi.org/10.1002/2016SW001375>
- Moretto, T., Olsen, N., Ritter, P., & Lu, G. (2002). Investigating the auroral electrojets with low altitude polar orbiting satellites. *Annales Geophysicae*, *20*(7), 1049–1061. <https://doi.org/10.5194/angeo-20-1049-2002>
- Newell, P. T., & Gjerloev, J. W. (2011). Substorm and magnetosphere characteristic scales inferred from the SuperMAG auroral electrojet indices. *Journal of Geophysical Research*, *116*, A12232. <https://doi.org/10.1029/2011JA016936>
- Newell, P. T., Sotirelis, T., & Wing, S. (2010). Seasonal variations in diffuse, monoenergetic, and broadband aurora. *Journal of Geophysical Research*, *115*, A03216. <https://doi.org/10.1029/2009JA014805>
- Olsen, N. (1996). A new tool for determining ionospheric currents from magnetic satellite data. *Geophysical Research Letters*, *23*(24), 3635–3638. <https://doi.org/10.1029/96GL02896>
- Olsen, N., & Stolle, C. (2017). Magnetic signatures of ionospheric and magnetospheric current systems during geomagnetic quiet conditions—An overview. *Space Science Reviews*, *206*, 5–25. <https://doi.org/10.1007/s11214-016-0279-7>
- Østgaard, N., Humberstet, B. K., & Laundal, K. M. (2011). Evolution of auroral asymmetries in the conjugate hemispheres during two substorms. *Geophysical Research Letters*, *38*, L03101. <https://doi.org/10.1029/2010GL046057>
- Østgaard, N., Reistad, J. P., Tenfjord, P., Laundal, K. M., Snekvik, K., Milan, S., & Haaland, S. (2016). Mechanisms that produce auroral asymmetries in conjugate hemispheres. In Y. Zhang, & L. J. Paxton (Eds.), *Auroral Dynamics and Space Weather Geophysical Monograph Series B* (Vol. 215, pp. 131–143). Hoboken, NJ: Wiley. <https://doi.org/10.1002/9781118978719.ch10>
- Pirjola, R. (2005). Space weather risk. *Space Weather*, *3*, S02A02. <https://doi.org/10.1029/2004SW000112>
- Pulkkinen, A., Amm, O., & Viljanen, A. (2003). Ionospheric equivalent current distributions determined with the method of spherical elementary current systems. *Journal of Geophysical Research*, *108*(A2), 1053. <https://doi.org/10.1029/2001JA005085>

- Ritter, P., Viljanen, A., Lühr, H., Amm, O., & Olsen, N. (2003). Ionospheric currents from CHAMP magnetic field data comparison with ground based measurements. In P. Ritter et al. (Eds.), *First CHAMP Mission Results Gravity, Magnetic and Atmospheric Studies* (pp. 347–352). Berlin: Springer. https://doi.org/10.1007/978-3-540-38366-6_50
- Russell, C. T., & McPherron, R. L. (1973). Semiannual variation of geomagnetic activity. *Journal of Geophysical Research*, 78(1), 92–108. <https://doi.org/10.1029/JA078i001p00092>
- Tenford, P., Østgaard, N., Snekvik, K., Laundal, K. M., Reistad, J. P., Haaland, S., & Milan, S. E. (2015). How the IMF B_y induces a B_y component in the closed magnetosphere and how it leads to asymmetric currents and convection patterns in the two hemispheres. *Journal of Geophysical Research: Space Physics*, 120, 9368–9384. <https://doi.org/10.1002/2015JA021579>
- Vennerstrom, S., & Moretto, T. (2013). Monitoring auroral electrojets with satellite data. *Space Weather*, 11, 509–519. <https://doi.org/10.1002/swe.20090>